Hydroxyapatite substituted by transition metals: experiment and theory

M. E. Zilm,†[a] L. Chen,†[a] V. Sharma,[a] A. McDannald,[a] M. Jain,[b] R. Ramprasad[a] and M. Wei*[a]

Bioceramics are versatile materials for hard tissue engineering. Hydroxyapatite (HA) is a widely studied biomaterial for bone grafting and tissue engineering applications. The crystal structure of HA allows for a wide range of substitutions, which allows for tailoring materials properties. Transition metals and lanthanides are of interest since substitution in HA can result in magnetic properties. In this study, experimental results were compared to theoretical calculations of HA substituted with a transition metal. Calculation of a 10 atomic percent substitution of a transition metal ion Mn^{2+}, Fe^{2+}, and Co^{2+} substituted HA samples lead to magnetic moments of 5, 4, and 3 Bohr magnetons, respectively. Hydroxyapatite substituted by transition metals (MHA) was fabricated through an ion exchange procedure and characterized with X-ray diffraction, Fourier transform infra-red spectroscopy (FTIR), X-ray photo-electron spectroscopy, and vibrating sample magnetometer, and results were compared to theoretical calculations. All the substitutions resulted in phase-pure $M^{2+}HA$ with lattice parameters and FTIR spectra in good agreement with calculations. Magnetic measurements revealed that the substitution of Mn^{2+} has the greatest effect on the magnetic properties of HA followed by the substitution of Fe^{2+} and then Co^{2+}. The present work underlines the power of synergistic theoretical–experimental work in guiding the rational design of materials.

1. Introduction

Hydroxyapatite (HA) is a commonly used bone grafting material and is a well-documented biomaterial known for its osteo-conductivity.[1,2] The main mineral phase of bone is HA, $Ca_{10}(PO_4)_6(OH)_2$, and its bioactivity can be modified through substitutions of other anions, cations, or functional groups. Well studied and commonly found trace elements in bone are Mg^{2+}, Sr^{2+}, CO_3^{2-}, and SiO_4^{4-}; these elements have been shown to render HA more bioactive compared to stoichiometric HA.[3–6] The hexagonal crystal structure of HA allows for a wide variety of substitutions that can alter bioactivity but also physical properties as well.[7] Other possible substituents which are less studied are transition metals of the 3d block, which are necessary for normal biological function.[8,9]

One unique characteristic of some transition metals is their magnetic response, one that can be modified and tuned in HA, which is diamagnetic, *via* substitutions. Thus, through substituting with magnetic ions HA with magnetic properties can be achieved resulting in a biocompatible and magnetic bio-material. There is a wide range of biomedical applications for biocompatible and magnetic materials such as drug delivery, cell separation, magnetic resonance imaging, and hyperthermia applications.[10–13] Iron oxide nanoparticles are currently used for these applications but there have been concerns over acute toxicity.[14] Since HA is biocompatible and biodegradable, application of magnetic HA will mitigate these concerns.

The most commonly used metal for imparting HA with magnetic properties is iron.[15–18] The choice of iron as a dopant stems from its high daily dietary need and its large magnetic moment. Other transition metals possess the potential and have rendered HA magnetic, such as cobalt,[19] but concerns over toxicity has limited the research despite the fact that cobalt is required in trace amounts for vitamin B12 function.[20] Another suitable transition metal that has received little attention is manganese, which has been shown to influence bone remodeling and is used as a supplement to retard bone loss.[21,22] However, initial studies have reported that manganese substitution does not affect the magnetic properties of HA.[23] Many elements have the potential to yield magnetic HA with varying levels of bioactivity and magnetization.

The time to synthesize and characterize all possible magnetic HAs is laborious and time consuming. The use of density functional theory (DFT) calculations to identify promising new

[a] *Department of Materials Science and Engineering, University of Connecticut, Storrs, CT, USA. E-mail: meiwei@engr.uconn.edu; Fax: +(860)486-4745; Tel: +(860)486-9253*

[b] *Department of Physics, University of Connecticut, Storrs, CT, USA*

† These authors contributed equally.

This journal is © the Owner Societies 2016

Phys. Chem. Chem. Phys., 2016, **18**, 16457–16465 | 16457

materials helps to guide and expedite experimental work. Computational efforts coupled with experimental work has provided information on site preference, structural modifications, and possible mechanisms of substitution in Pb, Cd, Sr, Mg, Zn, Ti, Si, CO_3^{2-}, and F.[24–34] In Si substituted HA, DFT has been used to study defect chemistry with results suggesting two different charge compensation mechanisms (1) the formation of $HSiO_4$ groups under hydrating conditions and (2) under dehydration the formation of OH vacancies, again DFT results coincided well with experimental data.[31,32] Material property changes have been successfully predicted with DFT in calcium deficient hydroxyapatite where Bhat *et al.* calculated a decrease of 30% in elastic properties due to calcium vacancies which coincided with observed experimental results.[35] Optical properties have also been calculated for the $Ca_{10}(PO_4)_6X_2$ system where X is OH, F, Cl, or Br with DFT and only minor differences in optical properties were calculated.[36] Theoretical work on magnetic HA systems have focused on the calculation of magnetic spectroscopic parameters for electron paramagnetic resonance (EPR) and Mössbauer spectras[37–40] Jiang *et al.* used DFT to analyze electronic structure and compute magnetic spectroscopic parameters for EPR and Mössbauer spectras of Fe^{2+} and Fe^{3+} substituted HA.[37] The comparison of experimental spectrums with computed spectroscopic parameters allowed for the assignment of site occupancy of Fe^{2+} and Fe^{3+} in the HA crystal lattice.[37] While EPR studies combined with DFT calculations have also helped understand interactions between nitrate and Mn^{2+} ions and nitrate and carbonate ions in the HA lattice where the nitrate ions are the paramagnetic center of interest.[38–40]

Little theoretical work has been done on the magnetic properties of HA substituted by divalent transition metals (MHA). Using DFT, we determined the most promising transition metals that would yield the highest magnetic moment, followed by synthesis of the substituted HAs. Herein we investigate the substitution of divalent transition metal ions: Mn^{2+}, Fe^{2+}, and Co^{2+} in HA from both theoretical and experimental approaches.

2. Materials and methods

2.1 Materials

Ammonium phosphate dibasic (99+%), iron chloride tetrahydrate (99+%), cobalt chloride hexahydrate (analysis grade), sulfuric acid (95–98%), and potassium bromide (IR grade) were purchased from Acros Organics. Calcium nitrate (99+%), manganese chloride tetrahydrate (99+%), lanthanum chloride heptahydrate (99+%), nitric acid (69.2%), and ammonium hydroxide (29.45%) were purchased from Fisher Scientific.

2.2 HA and MHA synthesis

HA was synthesized *via* a wet chemical method. An aqueous solution of ammonium phosphate dibasic (80 mM) was added drop-wise to an aqueous calcium nitrate solution (225 mM) at room temperature with the calcium to phosphate ratio maintained at 1.667. Ammonium hydroxide was used to raise the pH of both solutions above 11 prior to mixing the two solutions.

Once the two solutions were completely mixed, the temperature was raised to 95 °C and maintained at the temperature for five hours. Then the solution was cooled to room temperature and aged for two days under constant stirring. The precipitates were collected *via* centrifugation and washed 3 times with de-ionized, 2 times with ethanol and vacuum dried.

MHA samples were fabricated through an ion-exchange procedure. A salt solution of the desired transition metal ($MnCl_2$, $FeCl_2$, or $CoCl_2$) was prepared at a concentration of 0.02 M, and the pH of the solution was adjusted to 2.7 with dilute sulfuric acid. Previously synthesized HA was immersed in the ion-exchange solution at 0.5 g dL^{-1} and sonicated for one hour at room temperature with intermittent stirring. The ion-exchanged HA was collected by centrifugation, washed 3 times with DIW, and vacuum dried.

2.3 Characterization

Chemical analysis of the calcium and transition metal was determined by atomic absorption spectroscopy (Perkin Elmer Atomic Adsorption Spectrometer 3100). In brief, 15 mg of MHA powder was dissolved in 200 μL of concentrated nitric acid (15.9 M). A 2 M nitric acid solution with 5% (w/v) lanthanum chloride was then used to raise the total volume to 1 mL. The total volume was diluted to 20 mL with 0.1 M nitric acid and dilutions of the solution were used for chemical analysis.

Powder X-ray diffraction (XRD) patterns were acquired with a Bruker D2 phaser X-ray diffractometer operating at 30 kV and 10 mA using Cu Kα radiation. Diffraction patterns were collected over 2θ between 10–120° with a step size of 0.01° and a scan rate of 4 s per step. Powder patterns were refined using the Rietveld method with the general structural analysis system (GSAS) and the EXPGUI interface.[41,42]

FTIR spectra were acquired on a Nicolet Magna 560 FTIR spectrometer. Specimens were prepared using the potassium bromide method. In brief, powder samples were diluted to one part per million in KBr, grinded into a fine powder and then pressed into a transparent pellet. The FTIR spectra were acquired over the range of 4000–400 cm^{-1} with a resolution of 4 cm^{-1} and a total of 32 scans.

In order to assess the surface composition and oxidation state of the transition metal dopant, X-ray photoelectron spectroscopy (XPS) was employed using a VG X-ray Photoelectron Spectrometer with an Al Kα radiation source. High resolution XPS spectrums were acquired of the transition metal 2p and O 1s peaks using a pass energy of 50 eV and a step size of 0.1 eV. Spectrums were calibrated by setting the adventitious carbon peak to 284.7 eV, and CasaXPS was used to deconvolute the spectra.

Magnetic measurements were performed using a vibrating sample magnetometer (VSM) attached to the evercool physical property measurement system (from Quantum Design). Magnetization measurements were carried out at room temperature and with applied DC magnetic fields of up to 1 Tesla.

2.4 Theoretical calculations

Our DFT calculations were performed with the Vienna *ab initio* simulation package (VASP),[43] using the Perdew–Burke–Ernzerhof
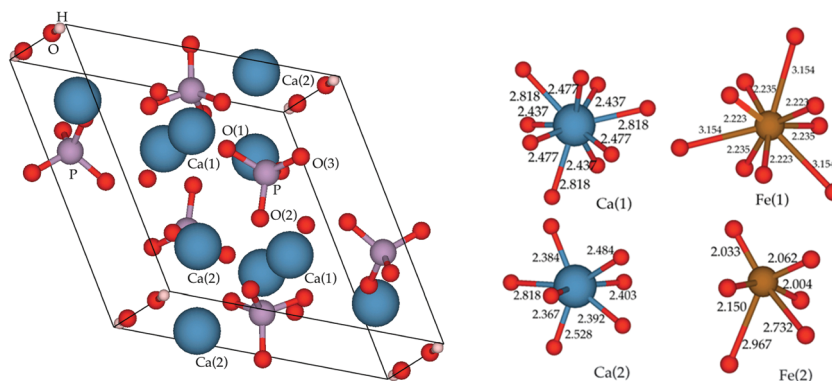
16458 | *Phys. Chem. Chem. Phys.,* 2016, **18**, 16457–16465

This journal is © the Owner Societies 2016

Fig. 1 On the left is the unit cell of hydroxyapatite from the calculated atomic positions. To the right of the unit cell is the local environment of Ca in pure HA and Fe in FeHA. Bond distances are in Å.

(PBE)[44] generalized gradient approximation (GGA) and a plane wave energy cutoff of 750 eV. Dense Monkhorst–Pack k-point meshes[45] of $2 \times 2 \times 2$ were used for sampling the Brillouin zone of HA. All atoms were allowed to relax to their equilibrium positions until atomic forces are smaller than 0.01 eV Å^{-1}.

3. Hydroxyapatite crystal structure

HA occurs in a hexagonal crystal structure (space group $P6_{3/m}$) with 44 atoms per unit cell and lattice parameters $a = b \neq c$ and $\alpha = \beta = 90°$, $\gamma = 120°$. The unit cell and the local environment of Ca in pure HA is depicted in Fig. 1. There are two distinct Ca sites where cation exchange may occur. The Ca(1) site is surrounded by nine oxygen ions from the surrounding phosphate tetrahedron and forms a distinct Ca channel parallel to the c-axis. The Ca(2) site is surrounded by six oxygen ions from five phosphate groups and the hydroxyl ion. The Ca(2) ions form triangular bases staggered by 60° above and below the OH ion. The OH ion similar to Ca(1) forms a distinct channel parallel to the c-axis. Based on the distance and the coordination number of oxygen and calcium, three oxygen atoms are defined as O(1), O(2) and O(3). The oxygen in OH$^-$ is defined as O$_H$. Thus the formula for HA can also be written as Ca(I)$_4$Ca(II)$_6$(PO(1)O(2)O(3)$_2$)$_6$(O$_H$H)$_2$.

The theoretical lattice constants from DFT calculation are $a = b = 9.55$ Å and $c = 6.94$ Å, which are in good agreement with the previously reported experimental values of HA: $a = b = 9.43$ Å, and $c = 6.88$ Å.[46] We also compare atomic positions and relaxed bond lengths in the unit cell with experimental and past DFT results for undoped HA in Tables 1 and 2. Our results are very close to the experimental data.[47] Based on Fig. 1, we note that there are six nearest neighboring oxygen atoms and three second nearest adjacent oxygen atoms for Ca(1), while Ca(2) has six nearest neighboring oxygen atoms and only one second nearest adjacent oxygen atom.

4. Results and discussion

The phase purity of the as-synthesized HA and MHA was evaluated using X-ray diffraction. Powder diffraction patterns of these

Table 1 Calculated atomic fractional coordinates of HA compare to literature values

Atom	This work			Other DFT[a]			Exp[b]		
	x	y	z	x	y	z	x	y	z
Ca(1)	0.333	0.667	0.004	0.333	0.667	0.003	0.333	0.667	0.001
Ca(2)	0.251	0.999	0.256	0.251	1	0.25	0.246	0.993	0.25
P	0.399	0.369	0.248	0.4	0.369	0.252	0.400	0.369	0.25
O(1)	0.332	0.486	0.251	0.333	0.487	0.253	0.329	0.484	0.25
O(2)	0.588	0.464	0.245	0.588	0.463	0.247	0.589	0.466	0.25
O(3)	0.34	0.257	0.068	0.338	0.256	0.073	0.348	0.259	0.073
OH	0	0	0.246	0	0	0.285	0	0	0.25

^{a} Ref. 55. ^{b} Ref. 46.

Table 2 Calculated bond lengths (Å) and bond angles (°) for HA compared to literature values

	This work	Other DFT[a]	Exp[b]
Bond length			
P–O(1)	1.550	1.541	1.533
P–O(2)	1.563	1.554	1.544
P–O(3)	1.551	1.545	1.514
Ca(1)–O(1)	2.437	2.425	2.416
Ca(1)–O(2)	2.477	2.469	2.449
Ca(1)–O(3)	2.817	2.827	2.802
Ca(2)–O(1)	2.818	2.798	2.712
Ca(2)–O(2)	2.366	2.357	2.356
Ca(2)–O(3)	2.391	2.367	2.367
Bond angles			
O(1)–P–O(2)	111		
O(1)–P–O(3)	111.8		
O(3)–P–O(2)	107.9		
O(1)–Ca(2)–O(2)	47.3		
O(1)–Ca(1)–O(2)	28.5		

^{a} Ref. 55. ^{b} Ref. 46.

samples are depicted in Fig. 2 along with the computed XRD patterns from the theoretical model, Fig. 3. The as-synthesized HA is identified with JCPDF 09-432 and the substituted HA do not exhibit any extraneous peaks, suggesting a single phase in all the powders. Rietveld refinements were performed on the synthesized powders using the refined atomic positions reported by Veselinovic *et al.*[48] The refined lattice parameters of HA and MHA are summarized in Table 3, which are in good
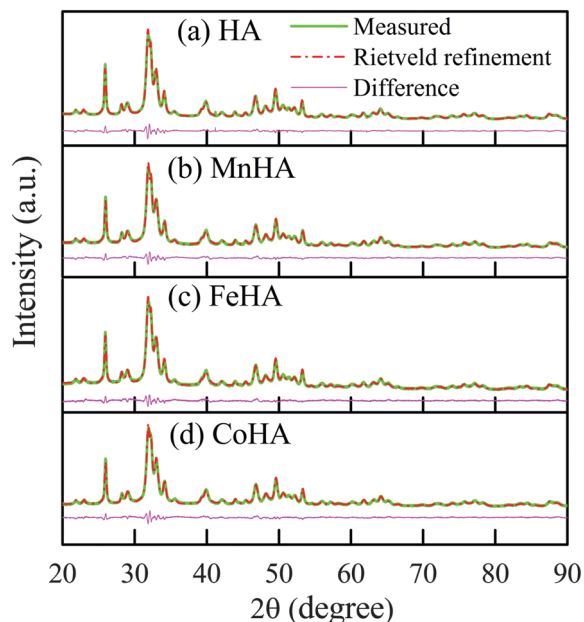
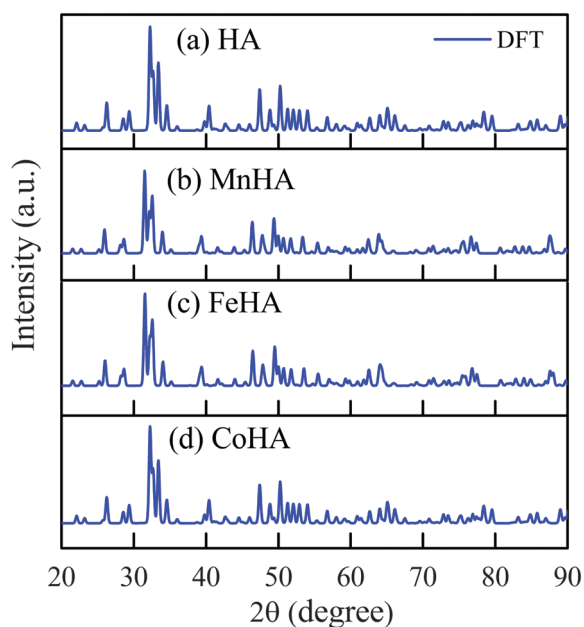Fig. 2 Powder XRD patterns of the synthesized HA and MHA. HA (a), MnHA (b), FeHA (c), and CoHA (d).

Fig. 3 Calculated XRD patterns from DFT calculations of HA and MHA: HA (a), MnHA (b), FeHA (c) and CoHA (d).

agreement with the calculated values from DFT calculations which assumed a 10 atomic percent substitution. The small differences in peak position between experimental and theoretical diffraction patterns arise from the differences in the calculated and observed lattice parameters. From atomic absorption spectroscopy, the M^{2+}/Ca ratios were determined to be 0.07, 0.12, and 0.05 for MnHA, FeHA, and CoHA, respectively. Energy dispersive X-ray spectroscopy was used to assess the stoichiometry of MHA, the (Ca + M^{2+})/P ratios were determined to be 1.72,

Table 3 Calculated geometry parameters of HA and M^{2+}HA for site (1) and site (2) substitutions. Experimental lattice parameters were obtained from Rietveld refinements. Units (Å)

System	Lattice constant	Site (1)	Site (2)	Exp
HA	a	9.55	—	9.4220(1)
	c	6.94	—	6.8867(8)
MnHA	a	9.32	9.47	9.4205(1)
	c	6.81	6.9	6.8805(9)
FeHA	a	9.52	9.38	9.4212(3)
	c	6.85	6.95	6.8841(2)
CoHA	a	9.50	9.52	9.4197(2)
	c	6.85	6.94	6.8820(1)

1.71, and 1.69 for MnHA, FeHA, and CoHA, which is in good agreement with the theoretical Ca/P ratio of 1.66, indicating that each M^{2+} ion replaces a Ca^{2+} ion. Changes in lattice parameters due to substitution are typically a function of the substituent percentage. Since the transition metal percentage was not controlled, it is difficult to directly compare the effect between transition metals on the lattice parameters.

Chemical analysis indicates that the transition metals successfully replaced calcium in the HA lattice. Between the two distinct calcium sites, DFT calculations indicate that the Ca(II) site is the most energetically favorable site for all calculated substitutions. Experimentally site occupancies cannot be reliably determined since diffraction data was not collected using synchrotron X-rays or with neutron diffraction. However, previous experimental and theoretical studies of Sr, Pb, and Cd substituted HA systems utilizing synchrotron radiation have shown that DFT does accurately predict the most energetically favorable site occupancy, where Ca(II) site is normally replaced by metal ions.[24–26]

To further understand the effect of transition metals on the structure of hydroxyapatite, DFT calculations were performed on the $Ca_9M(PO_4)_6(OH)_2$ (MHA) systems. Since the valence state of Ca^{2+} and M^{2+} are the same, charge compensation defects were not considered for M^{2+} substitution at the Ca(I) or Ca(II) sites. Table 3 displays the calculated lattice parameters of the MHA, which are in good agreement with data obtained from experiment. The contraction in the lattice parameters of MHA are attributed to the smaller ionic radius and the more electronegative character of Mn^{2+}, Fe^{2+}, and Co^{2+} compared to Ca^{2+}. These differences result in small structural distortions which is seen in the analysis of the interatomic distances of FeHA, shown in Fig. 1. The observed decrease of the bond length between the Fe and the first neighboring oxygen atoms results from iron being more electronegative than calcium attracting the oxygen atoms closer. The Fe at the Ca(2) results in one broke bond with oxygen, where the O(1) bond is broken.

The FTIR spectra of the pure and substituted HA are displayed in Fig. 4 along with the corresponding spectra computed using DFT. It can be seen that both results are in good agreement, indicating that the nearest neighbor environments and bond strengths are correctly captured in the DFT computations. There is a difference between the computed and experimental spectra. The error between the experimental and theoretical spectra for HA, MnHA, FeHA, CoHA, are 3.4%, 3.3%, 3.8%, and 4.1%, respectively. Overall, the theoretical and experimental
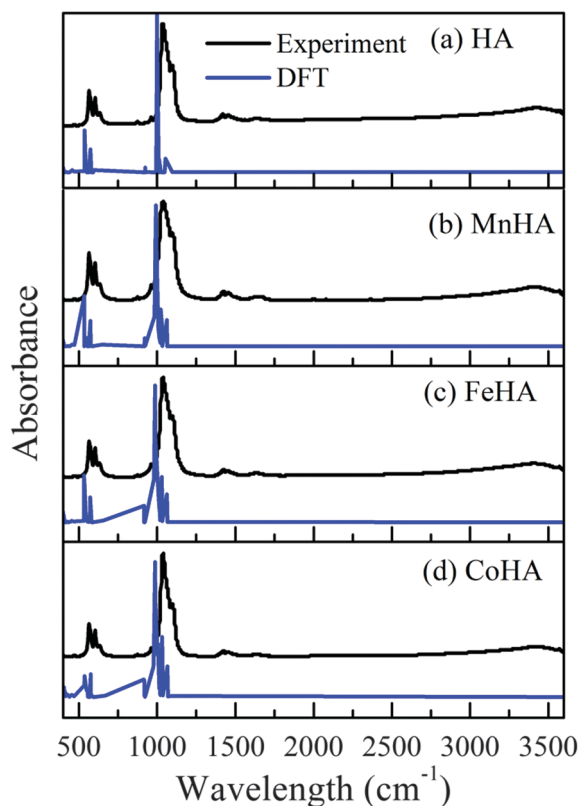
Fig. 4 FTIR spectra of the synthesized HA and MHA. HA (a), MnHA (b), FeHA (c), and CoHA (d).

spectra are in good agreement. Bhat *et al.* observed error ranging from 2% to 8% between theoretical and experimental spectra for stoichiometric HA.[35] Also, the theoretical model of a perfect crystal does not take into account defects such as vacancies that are often present in real samples. Bhat *et al.* calculated the IR spectra of calcium deficient HA and observed a shift in the vibrational modes of phosphate to lower wavenumbers.[35] The MHA spectra display typical vibrational modes of HA, indicating successful substitution of M^{2+} into the HA lattice. The vibrational modes of phosphate are observed around 1040 and 1095 cm^{-1} corresponding to the v3 mode, and the v4, v1, and v2 modes are present around 570, 600, and 480 cm^{-1}, respectively. The vibrational and liberation absorption bands for OH^- are observed around 3550 and 640 cm^{-1}, respectively, which are not predicted in the theoretical spectra. Other absorption bands observed in the experimental spectra that are not predicted by theory are the absorption bands observed at 1450, 1410, and 865 cm^{-1}, which correspond to the v3 and out of plane v2 mode for CO_3^{2-}. The presence of the CO_3^{2-} bands is a result of the HA synthesis procedure at ambient atmosphere. Carbonated HA is formed from the adsorption of CO_2 from the ambient atmosphere. From the position of the CO_3^{2-} bands the substitution of CO_3^{2-} is predominately at the phosphate site.

High resolution XPS spectra of the substituted transition metal in MHA, as shown in Fig. 5(a, c and e) and tabulated in Table 4, displays two peaks which are attributed to the $2p_{3/2}$ and $2p_{1/2}$ states from spin–orbit splitting.[49] For MnHA the peaks at 643.4 and 654.6 eV are the $2p_{3/2}$ and $2p_{1/2}$ peak pairs from the
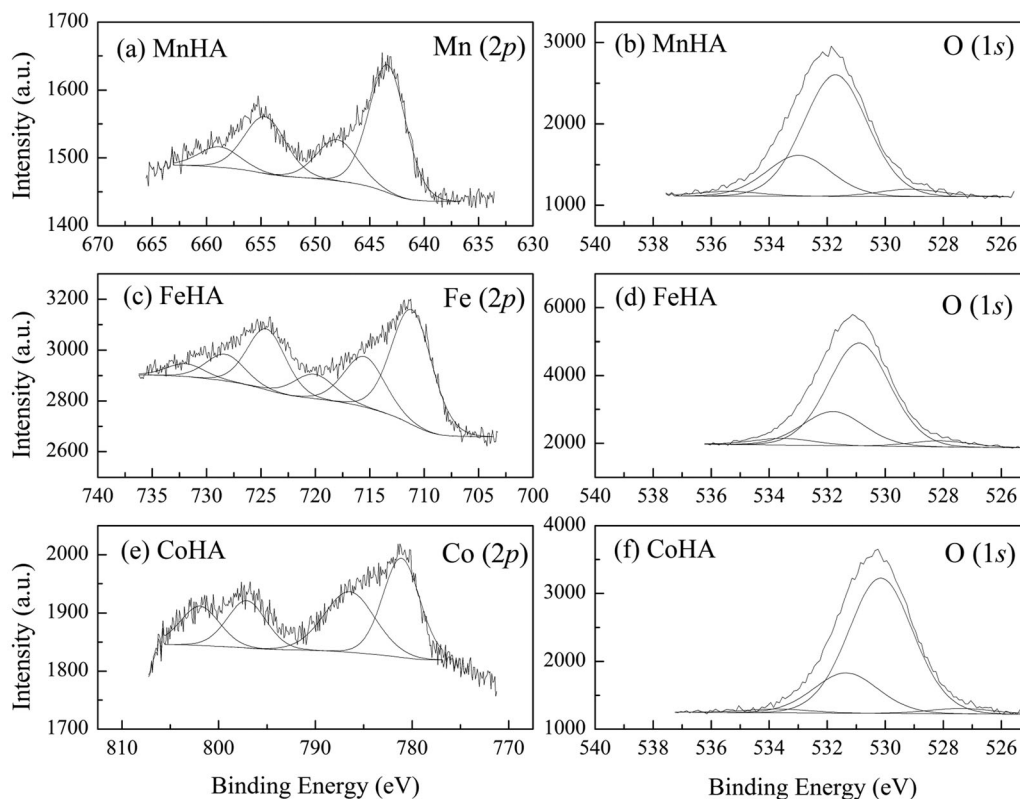

Fig. 5 XPS spectra of M 2p (left) and O 1s (right) peaks. MnHA (a and b), FeHA (c and d) and CoHA (e and f).
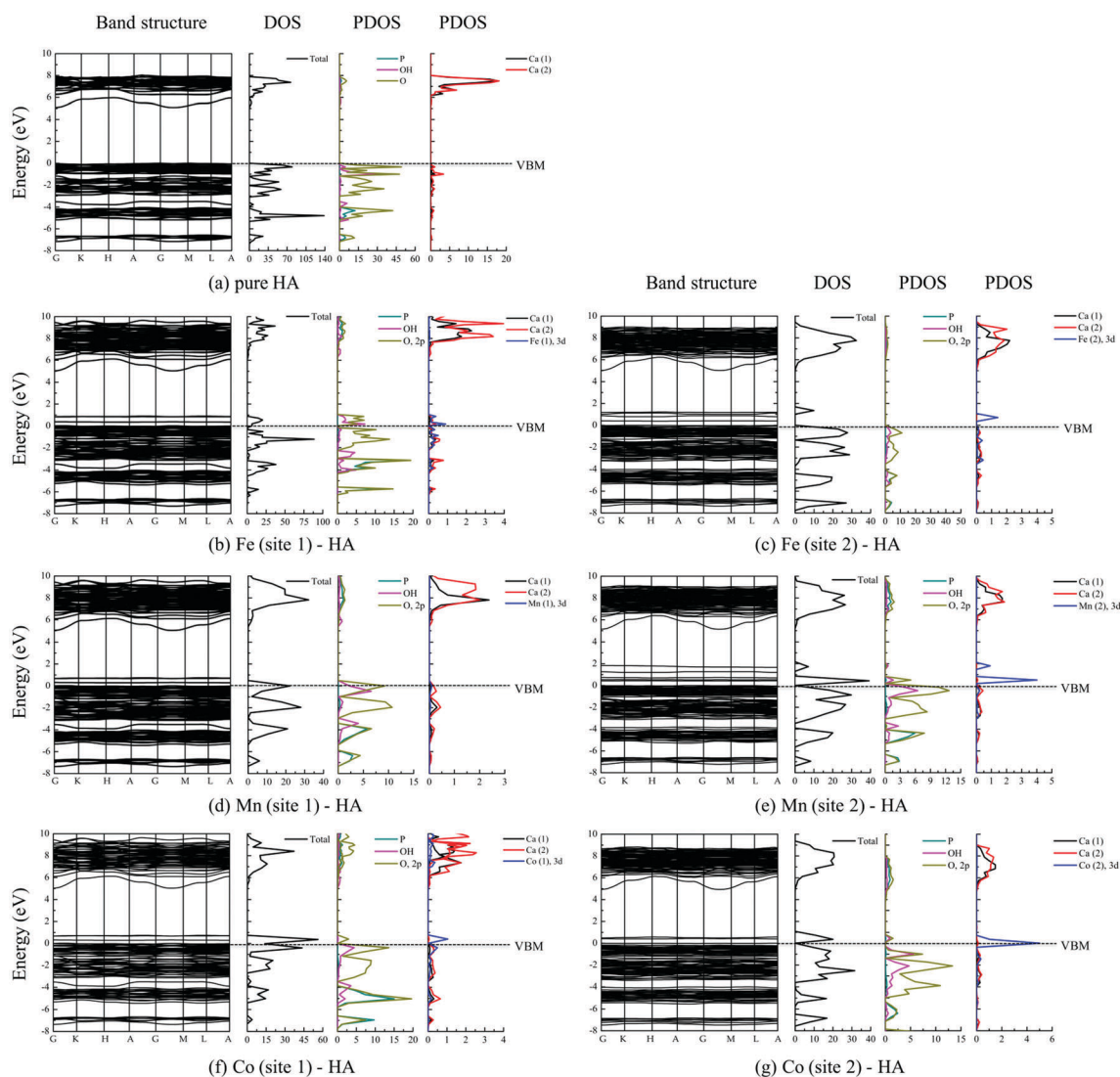
This journal is © the Owner Societies 2016

Phys. Chem. Chem. Phys., 2016, **18**, 16457–16465 | 16461

Table 4 Peak positions from deconvoluted MHA transitions metal (M) 2p spectra in eV

	M	
	$2p_{3/2}$	$2p_{1/2}$
MnHA	643.4, 648.0	654.6, 658.8
FeHA	711.1, 715.4, 720.1	724.5, 728.3, 731.9
CoHA	781.1, 786.5	797.1, 801.9

spin–orbit splitting, which corresponds with the Mn^{2+} substituted for Ca in the HA lattice.[50] The peaks at 648.0 and 658.8 eV are also 2p peak pairs, but are shakeup satellites of Mn^{2+}. In the case of CoHA the 2p peak pair at 781.1 and 797.1 eV corresponds to Co^{2+} substituted in either Ca site in the HA lattice and the 2p peak pair at 786.5 and 801.9 eV are from shakeup satellites. The strong nature of the shakeup satellite is characteristic of Co^{2+} with paramagnetic properties.[51] The peaks at 711.1 and 720.1 eV in the FeHA spectra are the 2p peak pairs from spin–orbit splitting

characteristic of $Fe^{2+}PO_4$ bonding, which corresponds to $Fe^{2+}HA$ in the lattice.[52] The 2p peak pair around 715.4 and 724.5 eV can be attributed to iron residing on surface sites, which requires more energy to create a photoelectron.[52] The last peak pair around 720.1 and 731.9 eV is a shakeup satellite of iron. The O 1s spectra were also acquired and all MHA displayed peaks around 528, 530, 531, and 533 eV. It should be noted that the peak at 531 eV is characteristic of O in HA (NIST database) and the peak around 530 eV is characteristic of surface carbonate (NIST database). The peak at 533 eV is typical of bridging oxygen's. The peak at 528 eV can be attributed to C–O bonding from the carbon tape used for mounting powders. No recognizable metal oxide bonding was identified in the transition metal 2p or O 1s spectra. All the paramagnetic transition metals appear to have successfully incorporated into the HA lattice in a divalent state.

XPS is successful at probing the electronic structure through core level electrons but does not provide information about the interactions in the valance band. To address this point,

Fig. 6 Projected density of states for MHA.

16462 | *Phys. Chem. Chem. Phys.,* 2016, **18**, 16457–16465

This journal is © the Owner Societies 2016

Table 5 Band gap of MHA, given in eV. The data in parenthesis is experimental results from literature

| System	Site (1)	Site (2)
HA	5.09	5.3[a]
MnHA	4.29	3.3
FeHA	4.15	3.8
CoHA	4.29	4.36

[a] Ref. 53.

we calculated the band structure and density of states, shown in Fig. 6, using DFT to further understand the effect of transition metals on the electronic properties of HA. The valance band maximum of HA is set as 0 eV in all figures, and the calculated PBE band gap of pure HA is 5.09 eV which is consistent with the previously computed result of 5.30 eV from Matsunaga *et al.*[53]

When the transition metals are substituted into HA, the band gap of the MHA decreases compared to pure HA as shown in Fig. 6 and Table 5. In order to describe the influence of specific atoms on the electronic structure of HA, density of states (DOS) and projected density of states analysis were performed, as shown in Fig. 6. Comparing to the partial DOS of pure HA, new energy states of ion-substituted HA are introduced at the top of the valence band owing to the interaction between 2p states of O and the 3d energy states of Fe, Co, and Mn. The interaction between these states results in decreasing the band gap in MHA.

Also, when Fe or Mn is substituted at the Ca(2) site, the band gap is smaller than substitution at the Ca(1) site. The structural distortion from Fe, Mn, and Co at site (1) is less compared to site (2) substitution. The coordination number of Fe, Mn, and Co at site (1) is the same as that of Ca(1), which is 9. Small variations of structure leads to extension of the band tail. However, the interaction between Fe (or Mn) at site (2) and the OH ion lead to the rotation of the OH ion, which results in the production of discrete states in the band structure of HA.

Magnetization measurements depicted in Fig. 7 show that all the substituents induced a transition from diamagnetic behavior, which is characteristic of HA, to a superparamagnetic behavior. A small ferromagnetic signal is observed at low magnetic fields followed by a strong paramagnetic response at high fields. The observed superparamagnetic response may be due to M^{2+} residing in Ca(2) sites or surface effects as previously discussed.[18] In brief, as the surface to volume ratio increases, a larger number of atoms reside on the surface possibly resulting in dangling bonds, a change in coordination and surface disorder, which can lead to an increase in their magnetization values.[54] The transition from diamagnetic to paramagnetic response is in agreement with the theoretical calculations. For a 10 percent substitution on the Ca-site, our theoretical modelling predicts magnetic moments of 5, 4 and 3 Bohr magnetons for MnHA, FeHA, and CoHA, respectively. Since the MHA fabricated by different approaches have varying levels of M^{2+} substituted into the lattice, magnetization curves were normalized to the molar amount of M^{2+} per MHA. In agreement with the calculations, MnHA displayed the highest magnetization value of 100 emu mol^{-1} M^{2+} at 10 kOe (or 1 Tesla) of all the substituents, while FeHA and CoHA had similar
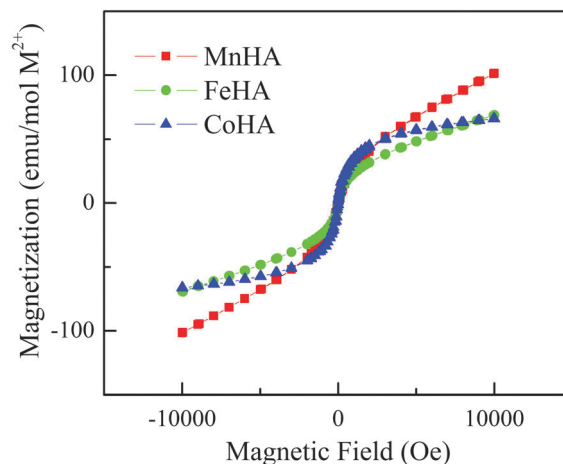
Fig. 7 Mass magnetization of MnHA, FeHA, and CoHA normalized to the transition metal content.

magnetization values around 65 emu mol^{-1} M^{2+}. Qualitatively, the slope of the high field magnetization data is also indicative of the magnitude of the magnetic moment and the observed slopes are MnHA > FeHA > CoHA, which is in good agreement with the theoretical calculations.

5. Conclusions

Manganese, iron and cobalt were successfully substituted into hydroxyapatite (HA) and the observed crystal structure, FTIR spectra, electronic and magnetic properties were in good agreement with DFT calculations. The presence of transition metals in a +2 oxidation state was confirmed by XPS, FTIR, and XRD identified the MHA without any detectable impurity phases. Incorporation of magnetic ions into the HA lattice was sufficient to induce a transition from the diamagnetic behavior (for pure HA) to a paramagnetic one, with the observed magnetization values in the order of MnHA > FeHA > CoHA.

The results from DFT calculations were in good agreement with experimental data. Thus, the DFT calculation could be a useful tool for predicting physical and magnetic properties of different ion-substituted hydroxyapatite powders, and such a tool can guide future studies on the synthesis of ion-substitute hydroxyapatite with desired properties.

Acknowledgements

References

1 W. Suchanek and M. Yoshimura, Processing and properties of hydroxyapatite-based biomaterials for use as hard tissue replacement implants, *J. Mater. Res.*, 1998, **13**, 94–117.

2   H. Zhou and J. Lee, Nanoscale hydroxyapatite particles for bone tissue engineering, *Acta Biomater.*, 2011, **7**, 2769–2781.

3   T. J. Webster, E. A. Massa-Schlueter, J. L. Smith and E. B. Slamovich, Osteoblast response to hydroxyapatite doped with divalent and trivalent cations, *Biomaterials*, 2004, **25**, 2111–2121.

4   W. Xue, J. L. Moore, H. L. Hosick, S. Bose, A. Bandyopadhyay, W. Lu, K. M. Cheung and K. D. Luk, Osteoprecursor cell response to strontium-containing hydroxyapatite ceramics, *J. Biomed. Mater. Res., Part A*, 2006, **79**, 804–814.

5   E. Landi, G. Celotti, G. Logroscino and A. Tampieri, Carbonated hydroxyapatite as bone substitute, *J. Eur. Ceram. Soc.*, 2003, **23**, 2930–2937.

6   N. Patel, S. M. Best, W. Bonfield, I. R. Gibson, K. A. Hing, E. Damien and P. A. Revell, A comparitive study on the *in vivo* behavior of hydroxyapatite and silicon substituted hydroxyapatite granules, *J. Mater. Sci.: Mater. Med.*, 2002, **13**, 1199–1206.

7   E. Boanini, M. Gazzano and A. Bigi, Ionic substitutions in calcium phosphates synthesized at low temperature, *Acta Biomater.*, 2010, **6**, 1882–1894.

8   S. Bose, G. Fielding, S. Tarfer and A. Bandyopadhyay, Understanding of dopant-induced osteogenesis and angiogenesis in calcium phosphate ceramics, *Trends Biotechnol.*, 2013, **31**, 594–605.

9   R. J. P. Williams, Role of transition metals in biological processes, *R. Inst. Chem., Rev.*, 1968, **1**, 13–38.

10 H. Xu, Z. P. Aguilar, L. Yang, M. Kuang, H. Duan, Y. Xiong, H. Wei and A. Wang, Antibody conjugated magnetic iron oxide nanoparticles for cancer cell separation in fresh whole blood, *Biomaterials*, 2011, **32**, 9758–9765.

11 H. B. Na, I. C. Song and T. Hyeon, Inorganic Nanoparticles for MRI Contrast Agents, *Adv. Mater.*, 2009, **21**, 2133–2148.

12 Q. A. Pankurst, J. Conolly, S. Jones and J. Dobson, Applications of magnetic nanoparticles in biomedicine, *J. Phys. D: Appl. Phys.*, 2003, **36**, R167–R181.

13 O. Veiseh, J. W. Gunn and M. Zhang, Design and fabrication of magnetic nanoparticles for targeted drug delivery and imaging, *Adv. Drug Delivery Rev.*, 2010, **62**, 284–304.

14 S. J. Soenen, U. Himmelreich, N. Nuytten and M. D. Cuyper, Cytotoxic effects of iron oxide nanoparticles and implications for safety in cell labeling, *Biomaterials*, 2011, **32**, 195–205.

15 V. S. Chandra, G. Baskar, R. V. Suganthi, K. Elayaraja, M. I. Ahymah Joshy, W. S. Beaula, R. Mythili, G. Venkatraman and S. N. Kalkura, Blood Compatibility of Iron-Dopen Nanosize Hydroxyapatite and Its Drug Release, *ACS Appl. Mater. Interfaces*, 2012, **4**, 1200–1210.

16 E. Kramer, M. Staruch, A. Morey-Oppenheim, M. Jain, J. Budnick, S. Suib and M. Wei, Synthesis and Characterization of Iron substituted Hydroxyapatite *via* a Simple Ion-Exchange Procedure, *J. Mater. Sci.*, 2013, **48**, 665–673.

17 S. Panseri, C. Cunha, T. D'Alessandro, M. Sandri, G. Giavaresi, M. Marcacci, C. T. Hung and A. Tampieri, Intrinsically superparamagnetic Fe-hydroxyapatite nanoparticles positively influence osteoblast-like cell behaviour, *J. Nanobiotechnol.*, 2012, **10**, 32.

18 M. E. Zilm, M. Staruch, M. Jain and M. Wei, An intrinsically magnetic biomaterial with tunable magnetic properties, *J. Mater. Chem. B*, 2014, **2**, 7176–7185.

19 E. Kramer, E. Itzkowitz and M. Wei, Synthesis and characterization of cobalt-substituted hydroxyapatite powders, *Ceram. Int.*, 2014, **40**, 13471–13480.

20 D. Lindsay and W. Kerr, Cobalt close-up, *Nat. Chem.*, 2011, **3**, 494.

21 Y. J. Bae and M. H. Kim, Manganese Supplementation Improves Mineral Density of the Spine and Femur and Serum Osteocalcin in Rats, *Biol. Trace Elem. Res.*, 2008, **124**, 28–34.

22 H. Rico, N. Gomez-Raso, M. Revilla, E. Hernandez, C. Seco and E. Crespo, Effects on bone loss of manganese alone or with copper supplement in ovariectomized rats A morphometric and densitomeric study, *Eur. J. Obstet. Gynecol. Reprod. Biol.*, 2000, **90**, 97–101.

23 Y. Li, J. Widodo, S. Lim and C. P. Ooi, Synthesis and cytocompatibility of manganese (II) and iron (III) substituted hydroxyapatite nanoparticles, *J. Mater. Sci.*, 2012, **47**, 754–763.

24 D. E. Ellis, J. Terra, O. Warschkow, M. Jiang, G. B. Gonzalez, J. S. Okasinski, M. J. Bedzyk, A. M. Rossi and J. G. Eon, A theoretical and experimental study of lead substitution in calcium hydroxyapatite, *Phys. Chem. Chem. Phys.*, 2006, **8**, 967–976.

25 J. Terra, G. B. Gonzalez, A. M. Rossi, J. G. Eon and D. E. Ellis, Theoretical and experimental studies of substitution of cadmium hydroxyapatite, *Phys. Chem. Chem. Phys.*, 2010, **12**, 15490–15500.

26 J. Terra, E. R. Dourado, J. G. Eon, D. E. Ellis, G. Gonzalez and A. M. Rossi, The structure of strontium-doped hydroxyapatite: an experimental and theoretical study, *Phys. Chem. Chem. Phys.*, 2009, **11**, 568–577.

27 J. Zeglinski, M. Nolan, M. Bredol, A. Schatte and S. A. M. Tofail, Unravelling the specific site preference in doping of calcium hydroxyapatite with strontium from *ab initio* investigations and rietveld analyses, *Phys. Chem. Chem. Phys.*, 2012, **14**, 3435–3443.

28 S. Yin and D. E. Ellis, First-principles investigations of Ti-substituted hydroxyapatite electronic structure, *Phys. Chem. Chem. Phys.*, 2010, **12**, 156–163.

29 D. Laurencin, N. Almora-Barrios, N. H. de Leeuw, C. Gervais, C. Bonhomme, F. Mauri, W. Chrzanowski, J. C. Knowles, R. J. Newport, A. Wong, Z. Gan and M. E. Smith, Magnesium incorporation into hydroxyapatite, *Biomaterials*, 2011, **32**, 1826–1837.

30 X. Ma and D. E. Ellis, Initial stages of hydration and Zn substitution/occupation on hydroxyapatite (0 0 0 1) surfaces, *Biomaterials*, 2008, **29**, 257–265.

31 R. Astala, X. Y. Caldren and M. J. Scott, Ab initio simulation of Si-doped hydroxyapatite, *Chem. Mater.*, 2006, **18**, 413–422.

32 H. F. Chappell and P. D. Bristowe, Density functional calculations of the properties of silicon-substituted hydroxyapatite, *J. Mater. Sci.: Mater. Med.*, 2006, **18**, 829–837.

33 R. Astala and M. J. Scott, First principles investigation of mineral component of bone: CO_3 substitutions in hydroxyapatite, *Chem. Mater.*, 2005, **17**, 4125–4133.

34 N. H. de Leeuw, Density functional theory calculations of local ordering of hydroxyl groups and fluoride ions in hydroxyapatite, *Phys. Chem. Chem. Phys.*, 2002, **4**, 3865–3871.

35 S. S. Bhat, U. V. Waghmare and U. Ramamurty, First-principles study of structure, vibrational, and elastic properties of stoichiometric and calcium-deficient hydroxyapatite, *Cryst. Growth Des.*, 2014, **14**, 3131–3141.

36 P. Rulis, L. Ouyang and W. Y. Ching, Electronic structure and bonding in calcium apatite crystals: hydroxyapatite, fluoroapatite, chloroapatite, bromoapatite, *Phys. Rev. B: Condens. Matter Mater. Phys.*, 2004, **70**, 155104.

37 M. Jiang, J. Terra, A. M. Rossi, M. A. Morales, E. M. Baggio Saitovitch and D. E. Ellis, Fe^{2+}/Fe^{3+} substitution in hydroxyapatite: theory and experiment, *Phys. Rev. B: Condens. Matter Mater. Phys.*, 2002, **66**, 224107.

38 M. Gafurov, T. Biktagirov, G. Mamin, E. Klimashina, V. Putlayev, L. Kuznetsova and S. Orlinskii, The interplay of manganese and nitrate in hydroxyapatite nanoparticles as revealed by pulsed EPR and DFT, *Phys. Chem. Chem. Phys.*, 2015, **17**, 20331–20337.

39 M. Gafurov, T. Biktagirov, G. Mamin and S. Orlinskii, A DFT, X- and W-band EPR and ENDOR study of nitrogen-centered species in (nano)hydroxyapatite, *Appl. Magn. Reson.*, 2014, **45**, 1189–1203.

40 T. Biktagirov, M. Gafurov, G. Mamin, E. Klimashina, V. Putlayev and S. Orlinskii, Combination of EPR measurements and DFT calculations to study nitrate impurities in the carbonated nanohydroxyapatite, *J. Phys. Chem. A*, 2014, **118**, 1519–1526.

41 A. C. Larson and R. B. Von Dreele, General Structure Analysis System (GSAS). *Los Alamos National Laboratory Report LAUR*, 2000, 86–748.

42 B. Toby, EXPGUI, a Graphical User Interface for GSAS, *J. Appl. Crystallogr.*, 2001, **34**, 210–213.

43 G. Kresse and J. Furthmuller, Efficient iterative schemes for *ab initio* total-energy calculations using plane-wave basis set, *Phys. Rev. B: Condens. Matter Mater. Phys.*, 1996, **54**, 11169.

44 J. Perdew, K. Burke and M. Ernzerhof, Generalized gradient approximation made simple, *Phys. Rev. Lett.*, 1996, **77**, 3865.

45 H. Monkhorst and J. Pack, Special points for Brillouin-zone integrations, *Phys. Rev. B: Condens. Matter Mater. Phys.*, 1976, **13**, 5188.

46 A. S. Posner, A. Perloff and A. F. Diorio, Refinement of the hydroxyapatite structure, *Acta Crystallogr.*, 1958, **11**, 308.

47 M. Methfessel and V. Fiorentini, Extracting convergent surface energies from slab calculations, *J. Phys.: Condens. Matter*, 1996, **8**, 6525.

48 L. Veselinovic, L. Karanovic, Z. Stojanovic, I. Bracko, S. Markovic, N. Ignatovic and D. Uskokovic, Crystal structure of cobalt-substituted calcium hydroxyapatite nanopowders prepared by hydrothermal processing, *J. Appl. Crystallogr.*, 2010, **43**, 320–327.

49 D. Briggs and M. Seah, *Practical surface analysis: by auger and X-ray photoelectron spectroscopy*, Wiler, Chichester, 1983.

50 I. Mayer, G. Peto, A. Karacs, G. Molnar and I. Popov, Divalent Mn in calcium hydroxyapatite by pulse laser deposition, *J. Inorg. Biochem.*, 2010, **104**, 1107–1111.

51 Y. Borod-ko, S. Vetchinkin, S. Zimont, I. Ivleva and Y. Shul'ga, Nature of satellites in X-ray photoelectron spectra XPS of paramagnetic cobalt (II) compounds, *Chem. Phys. Lett.*, 1976, **42**, 264–267.

52 M. Khachani, M. Kacimi, A. Ensuque, J. Piquemal, C. Connan, F. Bozon-Verduraz and M. Ziyad, Iron-calcium-hydroxyapatite catalysts: Iron speciation and comparative performances in butan-2-ol conversion and propane oxidative dehydrogenation, *Appl. Catal., A*, 2010, **388**, 113–123.

53 K. Matsunaga and A. Kuwabara, First-Principles study of vacancy formation in hydroxyapatite, *Phys. Rev. B: Condens. Matter Mater. Phys.*, 2007, **75**, 014102.

54 B. Issa, I. M. Obaidat, B. A. Albiss and Y. Haik, Magnetic Nanoparticles: Surface Effects and Properties Related to Biomedicine Applications, *Int. J. Mol. Sci.*, 2013, **26**, 21266–21305.

55 W. Zhu and P. Wu, Surface energetics of hydroxyapatite: a dft study, *Chem. Phys. Lett.*, 2004, **396**, 38–42.

This journal is © the Owner Societies 2016

Phys. Chem. Chem. Phys., 2016, **18**, 16457–16465 | 16465